Accepted Manuscript

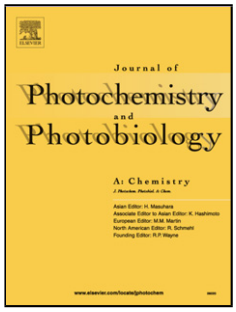

Title: Enhancement of photocatalytic activity of $CaTiO_3$ through HNO_3 acidification

Author: Chong Han Jingjing Liu Wangjin Yang Qianqian Wu He Yang Xiangxin Xue

PII: S1010-6030(15)30293-8
DOI: http://dx.doi.org/doi:10.1016/j.jphotochem.2016.02.012
Reference: JPC 10141

To appear in: *Journal of Photochemistry and Photobiology A: Chemistry*

Received date: 2-12-2015
Revised date: 11-2-2016
Accepted date: 15-2-2016

Please cite this article as: Chong Han, Jingjing Liu, Wangjin Yang, Qianqian Wu, He Yang, Xiangxin Xue, Enhancement of photocatalytic activity of CaTiO3 through HNO3 acidification, Journal of Photochemistry and Photobiology A: Chemistry http://dx.doi.org/10.1016/j.jphotochem.2016.02.012

This is a PDF file of an unedited manuscript that has been accepted for publication. As a service to our customers we are providing this early version of the manuscript. The manuscript will undergo copyediting, typesetting, and review of the resulting proof before it is published in its final form. Please note that during the production process errors may be discovered which could affect the content, and all legal disclaimers that apply to the journal pertain.

ACCEPTED MANUSCRIPT

Enhancement of photocatalytic activity of $CaTiO_3$ through HNO_3 acidification

Chong Han*, Jingjing Liu, Wangjin Yang, Qianqian Wu, He Yang, Xiangxin Xue

School of Metallurgy, Northeastern University, Shenyang, 110819, China

Abstract

$CaTiO_3$ synthesized by the hydrothermal method was treated to improve its photocatalytic activity using the HNO_3 acidification. Changes of morphology, structure, and composition of the acidified $CaTiO_3$ were investigated through various means such as XRD, SEM, BET, FTIR, Raman spectra, XPS, and UV-vis DRS. The results show that the enhancement of HNO_3 acidification led to the increase of substitutional N (O-Ti-N) compared to interstitial N (Ti-O-N and Ti-N-O) in the $CaTiO_3$ lattice. The apparent first-order reaction constant (k_{obs}) of methylene blue over the acidified $CaTiO_3$ at pH=2 was the largest and increased by 1.0 times than that over the not-acidified $CaTiO_3$, indicating that the acidified $CaTiO_3$ at pH=2 has the best photocatalytic performance among as-prepared samples. A negatively linear relationship between k_{obs} and $|1\text{-}N_{O\text{-}Ti\text{-}N}/N_{Ti\text{-}O\text{-}N+Ti\text{-}N\text{-}O}|$ suggests that the improvement of photocatalytic activity of $CaTiO_3$ by HNO_3 acidification depends on synergistic effects of substitutional and interstitial N in $CaTiO_3$ lattice.

Keywords: $CaTiO_3$; HNO_3; Substitutional N; Interstitial N

1. Introduction

The perovskite-type oxides with a structural formula of ABO_3 (A is a rare or alkaline earth metal and B is a first row transition metal) have excellent properties with wide applications in electronics, ceramics, superconductor, nonlinear optics, and catalysis [1-4]. $CaTiO_3$ is well known as one of the most important perovskites and has attracted more and more focus in the last decade. It can be prepared by many methods such as solid state [5-7], co-precipitation [8], mechanochemical [9], sol-gel [10-12], hydrothermal [13-16], and solvothermal methods [17, 18]. Among these methods, hydrothermal or solvothermal routes for $CaTiO_3$ have become the popular methods because they can exactly control crystal growth, achieve novel crystal

* Corresponding author. Tel.: +86-024-83684086; Fax: +86-024-83687719.
E-mail address: hanch@smm.neu.edu.cn (C. Han).

ACCEPTED MANUSCRIPT

morphologies, and optimize physicochemical properties [14]. Hydrothermal or solvothermal methods generally involved the facile reactions of titanium alkoxides or TiO_2, calcium salt, mineralizers, and water or organic solvent in a Teflon-lined stainless steel vessel at 100-220 ^oC [13-18].

Based on the hydrothermal method, rod-like and cubic-shaped $CaTiO_3$ particles were successfully synthesized by changing temperature and Ti-sources such as TiO_2 and titanium-triethanolamine [13]. Three-dimension aggregated prisms, butterfly-like dendrites, and cross cubic shapes $CaTiO_3$ particles were prepared by controlling NaOH concentration during the hydrothermal process [14]. Single-crystalline hollow $CaTiO_3$ cubes can be produced through introducing 5% water during the solvothermal process [18]. Spherical, cubic, and rectangular $CaTiO_3$ particles can be obtained with varying content (1.25%-5%) and addition order of water in the solvothermal process [17].

It has been widely reported that $CaTiO_3$ exhibits a superior photocatalytic performance in the removal of some organic and inorganic pollutants and the photolysis of water to hydrogen and oxygen [19-23]. The photodegradation percentage of methyl orange can reach to 96% using $CaTiO_3$ under ultraviolet light irradiation [12]. 98.4% of As(Ⅲ) was oxidized to As(Ⅴ) by photo-generated holes over fern-like $CaTiO_3$ nanoparticles [19]. Hydrogen production rate of 0.34 μmol/min was achieved with Pt-loaded $CaTiO_3$ as photocatalyst to decompose water [7]. $CaTiO_3$ shapes can affect its photocatalytic activity. Compared to flower-like and prism-like $CaTiO_3$, butterfly-like dendrites $CaTiO_3$ showed better photocatalytic activity to degrade rhodamine B [14]. Rectangular $CaTiO_3$ had higher activity than cubic and spherical ones for photocatalytic degradation of methylene blue [17].

Because of its wide band gap energy (3.5 eV), $CaTiO_3$ was photoactive only in ultraviolet light region. Recently, the metal doping has been made to enhance the photocatalytic activity of $CaTiO_3$. For example, the photocatalytic activity of Ag-La codoped $CaTiO_3$ for hydrogen evolution increased dramatically than that of $CaTiO_3$ when the doping amount was 3 mol% [10]. Compared to $CaTiO_3$, $CaTi_{1-x}Cu_xO_3$ ($0.1 \leq x \leq 0.04$) exhibited a higher activity for the photocatalytic decomposition of water to oxygen and hydrogen [11]. $Pt/CaTi_{0.9}Fe_{0.1}O_3$ had a certain activity while $Pt/CaTiO_3$ was inactive under visible light for photocatalytic generation of hydrogen from methanol-water solution [21]. Our previous study found that the doping of

ACCEPTED MANUSCRIPT

Fe in $CaTiO_3$ can promote the photocatalytic degradation of methylene blue [5].

In this study, $CaTiO_3$ synthesized using the hydrothermal method was modified to enhance its photocatalytic activity by HNO_3 acidification. The changes in the structures, compositions, and properties of the modified $CaTiO_3$ were detailedly characterized using various means including X-ray diffractometer (XRD), scanning electron microscope (SEM), specific surface area analysis, Fourier transform infrared spectrometer (FTIR), Raman spectrometer, X-ray photoelectron spectroscopy (XPS), and UV-vis diffuse reflection spectra (UV-vis DRS). The photocatalytic activity of $CaTiO_3$ was evaluated through the degradation of methylene blue (MB) under irradiation. Effects of HNO_3 acidification on the photocatalytic activity of $CaTiO_3$ were also discussed.

2. Experimental

2.1 $CaTiO_3$ synthesis

$CaTiO_3$ particles were synthesized by the hydrothermal method. In a typical process, solid $Ca(NO_3)_2 \cdot 4H_2O$ (2.362 g) was dissolved by water in the Teflon-lined stainless steel vessel. Tetrabutyl titanate (3.4 mL) was dropwise added into the solution under vigorous stirring. The molar ratio of Ca to Ti was 1.0. Then, solid NaOH (0.8 g) was introduced as the mineralization reagent. The mixture was continuously stirred at ambient temperature for 1.0 h. Subsequently, the hydrothermal treatment was carried out for 24 h at 200 ^oC. After cooling, the precipitates were recovered by the filtration, washed several times with ethanol, diluted acetic acid, and deionized water, and dried for 12 h at 80 ^oC.

2.2 HNO_3 acidification of $CaTiO_3$

The pH value of 20 mL deionized water was adjusted to 4 and 2, respectively, or the HNO_3 concentration in 20 mL deionized water was adjusted to 2 mol/L using HNO_3. These water solutions containing HNO_3 were used to modify $CaTiO_3$. After the addition of $CaTiO_3$ (0.2g), the corresponding acidic solution was continuously stirred to evaporate water at 50 ^oC. The sample was further dried for 24 h at 80 ^oC and then was calcined for 3 h at 500 ^oC. Thus, the acidified $CaTiO_3$ by HNO_3 at pH=4, pH=2, and HNO_3 concentration of 2 mol/L was obtained. As a comparison, the not-acidified $CaTiO_3$ was also likewise treated without the addition of HNO_3.

2.3 $CaTiO_3$ characterizations

ACCEPTED MANUSCRIPT

X-ray diffractometer (XRD, X' Pert Pro, PANalytical) with Cu Kα radiation at 40 kV and 40 mA was used to analyze crystal structures of $CaTiO_3$. A surface area & pore size analyzer (NOVA 1200e, Quantachrome) was employed to measure specific surface areas of $CaTiO_3$ by N_2 adsorption/desorption at 77 K. Specific surface areas were determined by applying the Brunauer-Emmett-Teller (BET) method to the adsorption isotherm in the partial pressure range of 0.05-0.35. Scanning electron microscope (SEM, SSX-550, SHIMADZU) was used to observe micro morphologies of $CaTiO_3$. Fourier transform infrared spectrometer (FTIR, Thermo Nicolet-380) was adopted to investigate functional groups of $CaTiO_3$ with KBr as a pelletizing medium. A UV resonance Raman spectrometer (UVR DLPC-DL-03) was used to obtain Raman spectra of $CaTiO_3$. The exciting radiation was a continuous diode pumped solid state (DPSS) laser beam (325 nm), and the source power output was 60 mW. A surface analysis system (ESCALAB 250, Thermo Fisher Scientific) with an Al Kα radiation was employed to record X-ray photoelectron spectroscopy (XPS) of $CaTiO_3$. The UV-vis diffuse reflection spectra (UV-vis DRS) of $CaTiO_3$ was recorded by a diffuse reflectance UV-vis spectrophotometer (2550, SHIMADZU) with $BaSO_4$ as the reflectance standard.

2.4 Photocatalytic activity test

The photocatalytic activity of $CaTiO_3$ was measured by decomposing MB in an aqueous solution under the irradiation of 500 W Xe lamp. During a typical MB removal experiment, $CaTiO_3$ (0.1 g) was dispersed into aqueous solution (200 mL) with initial MB concentration of 10 mg/L. Before irradiation, the aqueous suspension was magnetically stirred for 1.0 h to reach an adsorption/desorption equilibrium of MB on $CaTiO_3$ in the dark. Subsequently, the lamp was turned on and the photocatalytic activity test was performed at the temperature of 25 ^{o}C. Temporal changes of MB concentration were monitored by measuring the absorbance of the solution at 664 nm (the maximum absorption wavelength for MB) using the UV-vis spectrophotometer (UV-2550, SHIMADZU).

3. Results and discussion

3.1 Characterizations

Figure 1A shows XRD patterns of not-acidified and acidified samples. The peaks of not-acidified sample can be indexed to the standard XRD data of orthorhombic $CaTiO_3$ (JCPDS card No. 42-0423), determining that as-prepared sample through the hydrothermal

ACCEPTED MANUSCRIPT

method was assigned to well-crystallized $CaTiO_3$. The peaks at 2θ of 23.27°, 33.13°, 47.54°, 59.37°, 69.49°, and 79.25° can be related to (101), (121), (202), (123), (242), and (161) planes of orthorhombic $CaTiO_3$, respectively. After HNO_3 acidification at pH=4, pH=2, and 2 mol/L, peak positions and intensities of $CaTiO_3$ almost remained unchanged, implying that HNO_3 acidification did not introduce impurity phases. However, as shown in Figure 1B, a careful comparison in the range of 2θ=32-34° found that the peak positions of all acidified $CaTiO_3$ by HNO_3 slightly shifted towards a lower 2θ value. The ionic radius (0.171 nm) of N^{3-} is larger than the one (0.140 nm) of O^{2-}. According to the Bragg formula ($n\lambda=2d\sin\theta$, where n is diffraction series, λ is the X-ray wavelength, d is the crystalline plane distance, and θ is the diffraction angle), d value will increase when O^{2-} is substituted by N^{3-}, which can cause the distortion of $CaTiO_3$ crystal and result in the shift of peak positions in XRD patterns to lower 2θ values. This suggests that the N atom in HNO_3 may partially substitute the O atom in $CaTiO_3$ lattice. The crystallite sizes of $CaTiO_3$ were calculated using the Scherrer′ equation ($D=0.9\lambda/\beta\cos\theta$, where D is the crystallite size and β is the full width at half maximum (FWHM) of the most intense peak (121)). As summarized in Table 1, the crystallite sizes of not-acidified and acidified $CaTiO_3$ varied in the range of 43-44 nm, demonstrating the little effects of HNO_3 acidification on the crystallite sizes of $CaTiO_3$.

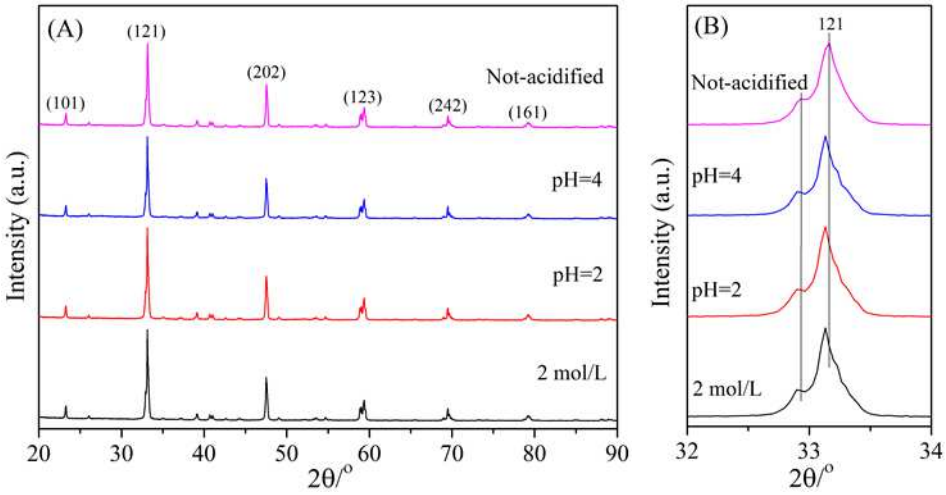

Figure 1 XRD patterns of not-acidified and acidified $CaTiO_3$

Figure 2 shows the morphologies of not-acidified and acidified $CaTiO_3$ particles by SEM.

ACCEPTED MANUSCRIPT

These images depicted that the morphologies and aggregate status of $CaTiO_3$ particles greatly varied with intensifying HNO_3 acidification. Not-acidified $CaTiO_3$ particles had irregular rectangular shapes, the surfaces of which undulated and ruptured to form step-like structures. Similar features were also observed for $CaTiO_3$ particles prepared by the hydrothermal progress of $Ca(NO_3)_2{\cdot}_4H_2O$ with $TiO(OH)_2$ from the hydrolysis of tetrabutyl titanate [19]. For the acidified $CaTiO_3$ particles at pH=4 and pH=2, only step-like structures with relative large sizes still existed while the ones with small sizes disappeared. Some very small particles adhered to the surface of step-like structures. The acidified $CaTiO_3$ particles at 2 mol/L even did not possess rectangular shapes and showed messy surfaces. These may be ascribed to the erosion role of HNO_3 in $CaTiO_3$ surface. As shown in Table 1, the specific surface area of not-acidified and acidified $CaTiO_3$ at pH=4, pH=2, and 2 mol/L was 16.92 m^2/g, 17.39 m^2/g, 16.14 m^2/g, and 14.90 m^2/g, respectively. This suggests that HNO_3 acidification has minor negative effects on the specific surface area of $CaTiO_3$.

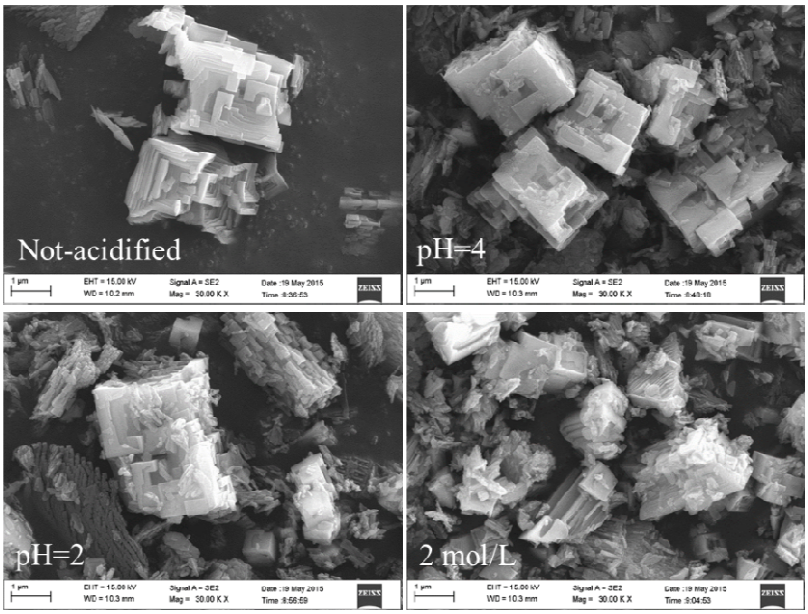

Figure 2 SEM images of not-acidified and acidified $CaTiO_3$

The functional groups of not-acidified and acidified $CaTiO_3$ were examined by FTIR spectra (Figure 3). The peaks at 440 and 554 cm^{-1} were related to Ti-O stretching and Ti-O-Ti bridge stretching modes [1, 24-26]. The peak at 1635 cm^{-1} belonged to the bending vibration of O-H band in hydroxyls and water adsorbed on $CaTiO_3$ surface [27-29]. Two N-O groups were observed in FTIR spectra. The band around 770 cm^{-1} and 1385 cm^{-1} can be assigned to

ACCEPTED MANUSCRIPT

the in-plane bending vibration of N-O (v_4) and the out-of-phase stretching vibration of N-O (v_3), respectively [30, 31]. HNO_3 acidification insignificantly affected functional groups of $CaTiO_3$.

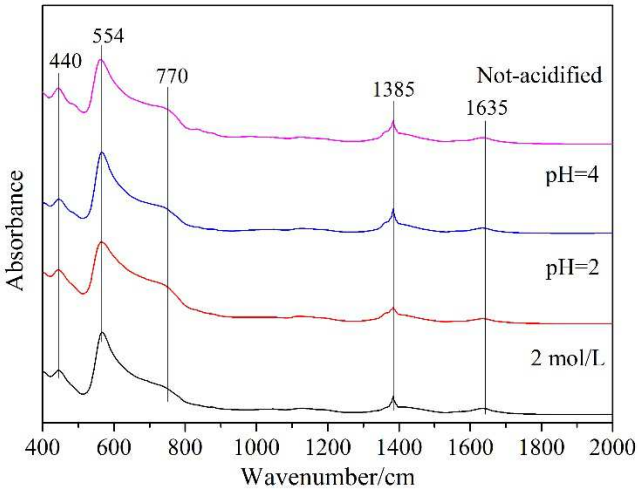

Figure 3 FTIR spectra of not-acidified and acidified $CaTiO_3$

Raman spectra was applied to have better insight into the functional groups of $CaTiO_3$. As shown in Figure 4, functional groups including Ti-O and O-Ti-O (445 cm^{-1}), N-O (721 cm^{-1} and 1348 cm^{-1}), and O-H (1630 cm^{-1}) that were detected in FTIR spectra were also observed in Raman spectra [32-35]. Contrasted to the peaks in FTIR spectra, it was noticed that two new bands at 848 cm^{-1} and 1042 cm^{-1} appeared in Raman spectra, which can be assigned to the out-of-plane deformation N-O (v_2) and the in-phase stretching vibration of N-O (v_1), respectively [34, 35]. Generally, v_1 is Raman active, v_2 is infrared active, and v_3 and v_4 are both Raman and infrared active [30, 34]. Nevertheless, the v_2 may become Raman active due to the changes of its presence environment [30, 35]. Therefore, both of v_3 and v_4 were found in FTIR and Raman spectra while v_1 and v_2 was observed only in Raman spectra. Additionally, all peak intensities of acidified $CaTiO_3$ at pH=2 and 2 mol/L were higher than that for not-acidified $CaTiO_3$ and acidified $CaTiO_3$ at pH=4. The morphology and crystal size of materials can strongly affect the strength of Raman signal because they can influence the ratio of absorption and scattering events [36-40]. Here, the morphology enhancement effect may be responsible for the increase of Raman peak intensities because the morphology of $CaTiO_3$ particles greatly varied but the crystal size almost remained unchanged with HNO_3 acidification.

ACCEPTED MANUSCRIPT

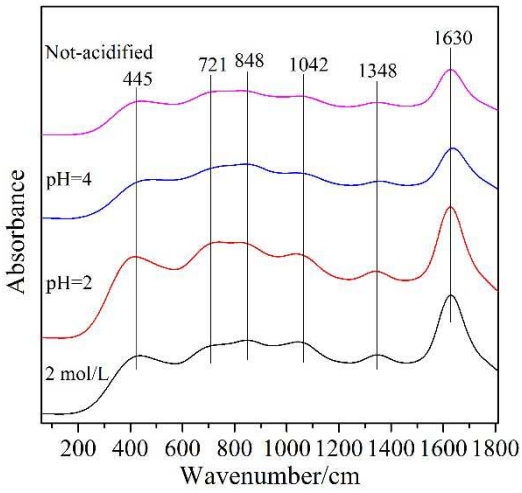

Figure 4 Raman spectra of not-acidified and acidified $CaTiO_3$

The chemical compositions and states of surface elements in not-acidified and acidified $CaTiO_3$ were investigated by XPS spectra. As seen in Figure 5, Ti 2p XPS spectra showed two peaks at the binding energy of 456.8-457.6 eV and 462.6-463.4 eV, which are assigned to Ti^{4+} $2p^{3/2}$ and Ti^{4+} $2p^{1/2}$, respectively [41-44]. There exhibited no shoulder at lower binding energies that are classically attributed to Ti^{3+} due to oxygen vacancies [45], indicating the existence of only Ti^{4+} in all $CaTiO_3$ samples. Additionally, the binding energies of Ti^{4+} $2p^{3/2}$ and Ti^{4+} $2p^{1/2}$ in acidified $CaTiO_3$ shifted to higher values compared with that in not-acidified $CaTiO_3$. This indicates different electronic interactions of Ti^{4+} and other ions and may be related to a decrease in the electron density around Ti atom because of HNO_3 acidification [27, 40, 46, 47]. It was speculated that the substitute element may be permeated into the acidified $CaTiO_3$ lattice.

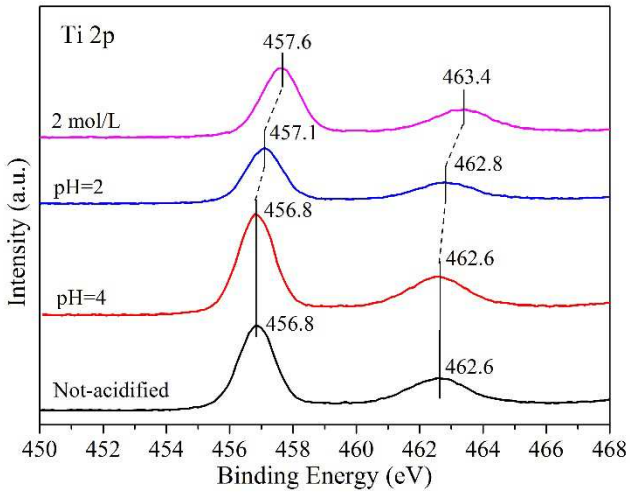

Figure 5 Ti 2p XPS spectra of not-acidified and acidified $CaTiO_3$

ACCEPTED MANUSCRIPT

Figure 6 shows O 1s XPS spectra of not-acidified and acidified $CaTiO_3$. O 1s XPS spectra can be fitted into a main peak at 527.9-528.6 eV and a shoulder peak around 529.4-530.3 eV. The fitting results coincided well with experimental spectra and were credible. The former belonged to oxygen in the $CaTiO_3$ lattice and the latter corresponded to oxygen in surface OH groups [29, 41, 42]. Compared to that for not-acidified and acidified $CaTiO_3$ at pH=4, the two peaks of O 1s for the acidified $CaTiO_3$ at pH=2 and 2 mol/L positively shifted by 0.3-0.7 eV and 0.1-0.9 eV. This may be attributed to a little adsorbed nitrate at high HNO_3 concentration since O 1s peaks in nitrate usually appear at 532.6-533.6 eV [42].

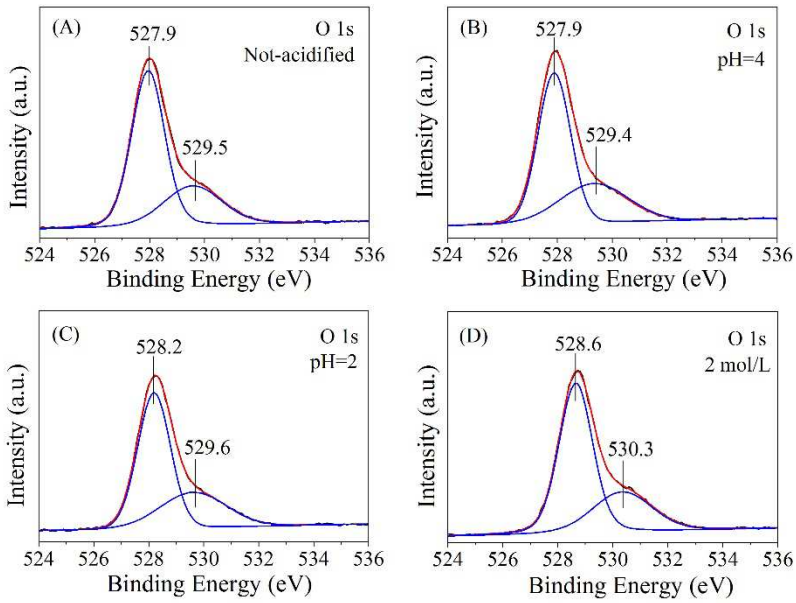

Figure 6 O 1s XPS spectra of not-acidified and acidified $CaTiO_3$. (A) not-acidified $CaTiO_3$; (B) acidified $CaTiO_3$ at pH=4; (C) acidified $CaTiO_3$ at pH=2; (D) acidified $CaTiO_3$ at 2 mol/L.

Figure 7 shows N 1s XPS spectra of not-acidified and acidified $CaTiO_3$. There was a broad N 1s peak in the range of 386-404 eV. After curve fitting, two peaks can be obtained around 392.1-394.1 eV and 396.8-398.9 eV, respectively. The fitting results were well coincident with experimental spectra and were believable. The peak at the lower binding energy was assigned to the substitutional N in the O-Ti-N linkages by the replacement of oxygen atom in $CaTiO_3$ lattice, and the other peak at the higher binding energy was ascribed to the interstitial N in the forms of Ti-O-N and Ti-N-O [41, 44, 47, 48]. Thus, the substitutional and interstitial

ACCEPTED MANUSCRIPT

states of N coexisted in all $CaTiO_3$ samples. The molar ratio of O-Ti-N to Ti-O-N and Ti-N-O ($N_{O\text{-}Ti\text{-}N}/N_{Ti\text{-}O\text{-}N+Ti\text{-}N\text{-}O}$) was 0.62, 0.77, 0.91, and 1.18, respectively, for not-acidified $CaTiO_3$ and acidified $CaTiO_3$ at pH=4, pH=2, and 2 mol/L. It indicates that the enhancement of HNO_3 acidification mainly results in the increase of amount of substitutional N in $CaTiO_3$ lattice. Besides, the third weak N 1s peak was also observed at 405.9 and 406.4 eV for the acidified $CaTiO_3$ at pH=2 and 2 mol/L, which was related to the N in the adsorbed NO_3^- on $CaTiO_3$ surface [42, 49, 50]. The adsorbed N, which only accounted for 3.0-5.0% of total N, should have a slight contribution to the signals of N-O bands in FTIR and Raman spectra (Figure 3 and 4). The results of N 1s XPS spectra can well explain the shift of peaks in XRD patterns. Figure 7A demonstrates that the hydrothermal process can cause the permeation of N from Ca source ($Ca(NO_3)_2 \cdot 4H_2O$) into $CaTiO_3$ lattice and then generate N-doped $CaTiO_3$, which has been never reported in previous papers using the hydrothermal method with $Ca(NO_3)_2 \cdot 4H_2O$ as Ca source to prepare $CaTiO_3$ [17, 19]. For acidified $CaTiO_3$ (Figure 7B-D), substitutional and interstitial N may originate from $Ca(NO_3)_2 \cdot 4H_2O$ and HNO_3 while the adsorbed N only emerged from HNO_3.

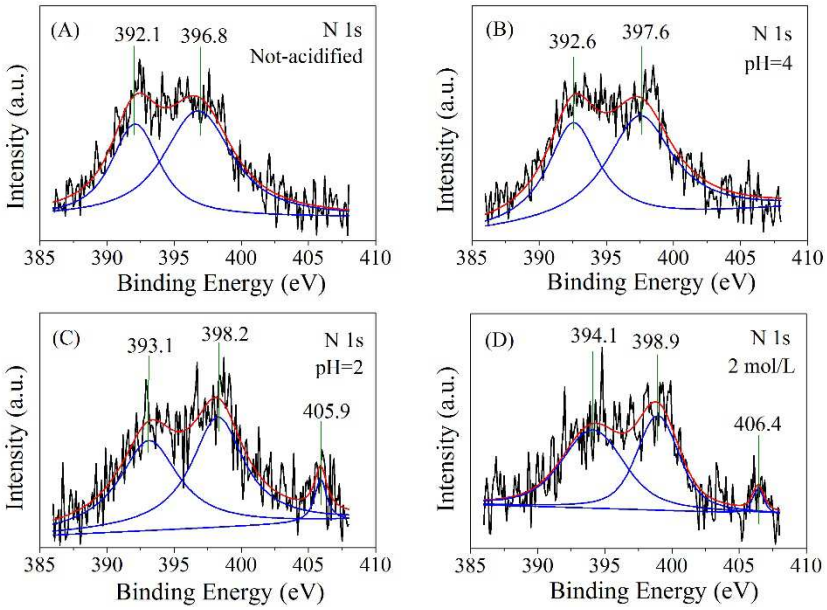

Figure 7 N 1s XPS spectra of not-acidified and acidified $CaTiO_3$. (A) not-acidified $CaTiO_3$; (B) acidified $CaTiO_3$ at pH=4; (C) acidified $CaTiO_3$ at pH=2; (D) acidified $CaTiO_3$ at 2 mol/L.

Figure 8A displays UV-vis DRS of not-acidified and acidified $CaTiO_3$. Compared with

ACCEPTED MANUSCRIPT

not-acidified $CaTiO_3$, acidified $CaTiO_3$ at pH=4 and pH=2 showed a stronger adsorption in the region of 350-410 nm and their adsorption edges exhibited a slight red-shift. According to XPS results (Figure 7B and C), the red-shift of adsorption edge may be related to the increase of substitutional N in $CaTiO_3$ lattice with increasing acidity. Substitutional N can lead to a narrower bandgap by mixing with O2p states and generate an isolated state above the valence band [47, 51-53]. Nevertheless, acidified $CaTiO_3$ at 2 mol/L displayed a blue-shift of the adsorption edge compared to acidified $CaTiO_3$ at pH=2, and it had similar light adsorption properties to not-acidified $CaTiO_3$. Although the acidified $CaTiO_3$ at 2 mol/L contained more substitutional N (Figure 7D), there may be the optimum amount of substitutional N to accomplish the narrowest bandgap and the best photoresponsive ability. $CaTiO_3$ is an indirect inter-band transition material [2]. As shown in Figure 8B, the bandgap of $CaTiO_3$ can be calculated by plotting $(F(R_\infty)h\nu)^{1/2}$ ($F(R_\infty)=(1-R_\infty)^2/2R_\infty$, R_∞ is diffuse reflectance, and $h\nu$ is the photon energy) versus the energy of absorbed light. The bandgap energy of not-acidified $CaTiO_3$ and acidified $CaTiO_3$ pH=4, pH=2, and 2 mol/L was 3.50 eV, 3.46 eV, 3.42 eV, and 3.51 eV (Table 1), respectively.

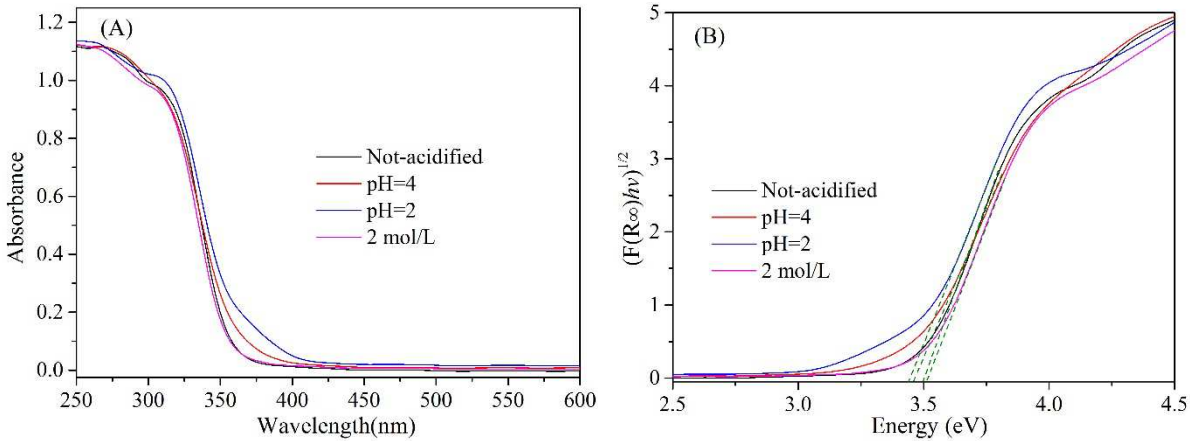

Figure 8 UV-vis spectra (A) and plots of transformed Kubelka-Munk function versus the energy of absorbed light (B) for not-acidified and acidified $CaTiO_3$

3.2 Photocatalytic activity

The Langmuir-Hinshelwood kinetic model was usually used to describe the photocatalytic degradation process of MB by catalysts [2, 43, 47]. The first-order reaction kinetic function was expressed as $\ln(C_t/C_0)=k_{obs}t$, where C_0 is initial MB concentration, C_t was the MB

ACCEPTED MANUSCRIPT

concentration at the irradiation time *t*, and k_{obs} is the apparent first-order reaction constant. Figure 9 shows photocatalytic degradation kinetics of MB. Plots of $\ln(C_t/C_0)$ with *t* exhibited a well linear relationship, determining that the photocatalytic degradation of MB by $CaTiO_3$ followed pseudo first-order kinetics. The k_{obs} of MB self-degradation was $(1.09\pm0.03)\times10^{-3}$ min^{-1}. The k_{obs} of MB degradation over not-acidified $CaTiO_3$ was $(1.80\pm0.04)\times10^{-3}$ min^{-1} while it was $(2.46\pm0.08)\times10^{-3}$ min^{-1}, $(3.59\pm0.05)\times10^{-3}$ min^{-1}, and $(3.10\pm0.10)\times10^{-3}$ min^{-1}, respectively, for MB degradation over acidified $CaTiO_3$ at pH=4, pH=2 and 2 mol/L. All acidified $CaTiO_3$ had higher photocatalytic activity than not-acidified $CaTiO_3$. The k_{obs} of MB over acidified $CaTiO_3$ at pH=2 was the largest and increased by 1.0 times compared to that over not-acidified $CaTiO_3$, confirming that acidified $CaTiO_3$ at pH=2 exhibits the best photocatalytic activity among as-prepared samples.

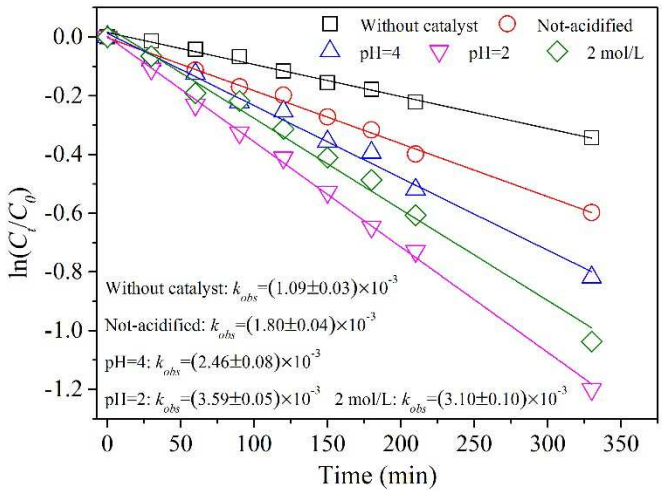

Figure 9 Photocatalytic degradation kinetics of MB over not-acidified and acidified $CaTiO_3$

As shown in Figure 7, the enhancement of HNO_3 acidification caused the increase of the ratio of O-Ti-N to Ti-O-N and Ti-N-O ($N_{O\text{-}Ti\text{-}N}/N_{Ti\text{-}O\text{-}N+Ti\text{-}N\text{-}O}$). Furthermore, the substitutional N in the O-Ti-N linkages and the interstitial N in the forms of Ti-O-N and Ti-N-O can play important roles in the light adsorption ability and the photocatalytic activity of materials [41, 44, 47, 48]. Therefore, the quantitative relationship of $N_{O\text{-}Ti\text{-}N}/N_{Ti\text{-}O\text{-}N+Ti\text{-}N\text{-}O}$ and photocatalytic activity may be attempted to be built. Figure 10 displays the plots of k_{obs} versus the absolute value of subtraction of 1 and $N_{O\text{-}Ti\text{-}N}/N_{Ti\text{-}O\text{-}N+Ti\text{-}N\text{-}O}$ ($|1\text{-}N_{O\text{-}Ti\text{-}N}/N_{Ti\text{-}O\text{-}N+Ti\text{-}N\text{-}O}|$). Interestingly, the k_{obs} and $|1\text{-}N_{O\text{-}Ti\text{-}N}/N_{Ti\text{-}O\text{-}N+Ti\text{-}N\text{-}O}|$ exhibited a negatively linear relationship with a math equation of $k_{obs}=-(6.11\pm0.60)\times10^{-3}\times|1\text{-}N_{O\text{-}Ti\text{-}N}/N_{Ti\text{-}O\text{-}N+Ti\text{-}N\text{-}O}|+(4.10\pm0.17)\times10^{-3}$, meaning that

ACCEPTED MANUSCRIPT

$CaTiO_3$ would have the highest photocatalytic activity when $N_{O\text{-}Ti\text{-}N}/N_{Ti\text{-}O\text{-}N+Ti\text{-}N\text{-}O}$ is equal to 1. These confirm that the improvement of photocatalytic activity of $CaTiO_3$ though HNO_3 acidification significantly depends on synergistic effects of substitutional and interstitial N in $CaTiO_3$ lattice.

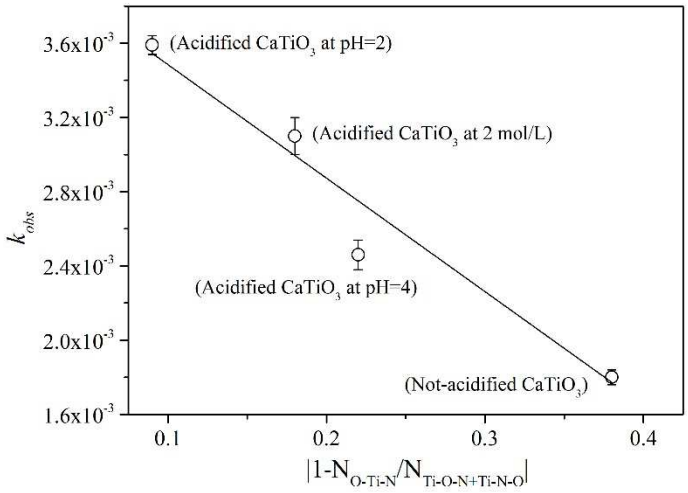

Figure 10 Plots of k_{obs} versus $|1\text{-}N_{O\text{-}Ti\text{-}N}/N_{Ti\text{-}O\text{-}N+Ti\text{-}N\text{-}O}|$

4. Conclusions

HNO_3 acidification had little effects on the crystallite sizes and specific surface areas of $CaTiO_3$ while it can destroy step-like structures on $CaTiO_3$ surface. FTIR and Raman spectra detected functional groups Ti-O, Ti-O-Ti and N-O. Ti 2p and O 1s XPS spectra confirmed the existence of Ti^{4+} and O in the $CaTiO_3$ lattice and surface OH groups in not-acidified and acidified $CaTiO_3$. N 1s XPS spectra suggested that substitutional N in the O-Ti-N linkages and interstitial N in the forms of Ti-O-N and Ti-N-O coexisted in not-acidified and acidified $CaTiO_3$. The enhancement of HNO_3 acidification increased the amount of substitutional N in $CaTiO_3$ lattice. The acidified $CaTiO_3$ at pH=4 and pH=2 showed a stronger adsorption in the region of 350-410 nm and a slight red-shift of their adsorption edges. The k_{obs} of MB over acidified $CaTiO_3$ at pH=2 increased by 1.0 times compared to that over not-acidified $CaTiO_3$, suggesting that acidified $CaTiO_3$ at pH=2 has the best photocatalytic activity. The k_{obs} and $|1\text{-}N_{O\text{-}Ti\text{-}N}/N_{Ti\text{-}O\text{-}N+Ti\text{-}N\text{-}O}|$ exhibited a negatively linear relationship, which confirms that the improvement of photocatalytic activity of $CaTiO_3$ by HNO_3 acidification is dependent on synergistic effects of substitutional and interstitial N in $CaTiO_3$ lattice.

ACCEPTED MANUSCRIPT

Acknowledgements

This research was financially supported by the National Natural Science Foundation of China (21407020) and the Fundamental Research Fund for the Central Universities (N130302004).

References

[1] L.M. Lozano-Sánchez, S.W. Lee, T. Sekino, V. Rodríguez-González, Practical microwave-induced hydrothermal synthesis of rectangular prism-like $CaTiO_3$, Cryst. Eng. Comm. 15 (2013) 2359-2362.

[2] M. Ye, M. Wang, D. Zheng, N. Zhang, C. Lin, Z. Lin, Garden-like perovskite superstructures with enhanced photocatalytic activity, Nanoscale 6 (2014) 3576-3584.

[3] Y. Li, X.P. Gao, G.R. Li, G.L. Pan, T.Y. Yan, H.Y. Zhu, Titanate Nanofiber Reactivity: Fabrication of $MTiO_3$ (M = Ca, Sr, and Ba) Perovskite Oxides, J. Phys. Chem. C 113 (2009) 4386-4394.

[4] W. Dong, B. Li, Y. Li, X. Wang, L. An, C. Li, B. Chen, G. Wang, Z. Shi, General Approach to Well-Defined Perovskite $MTiO_3$ (M = Ba, Sr, Ca, and Mg) Nanostructures, J. Phys. Chem. C 115 (2011) 3918-3925.

[5] H. Yang, C. Han, X. Xue, Photocatalytic activity of Fe-doped $CaTiO_3$ under UV-visible light, J. Environ. Sci. 26 (2014) 1489-1495.

[6] M. Shivaram, R.H. Krishna, H. Nagabhushana, S.C. Sharma, B.M. Nagabhushana, B.S. Ravikumar, N. Dhananjaya, C. Shivakumara, J.L. Rao, Synthesis, characterization, EPR and thermoluminescence properties of $CaTiO_3$ nanophosphor, Mater. Res. Bull. 48 (2013) 1490-1498.

[7] K. Shimura, H. Yoshida, Hydrogen production from water and methane over Pt-loaded calcium titanate photocatalyst, Energ. Environ. Sci. 3 (2010) 615-617.

[8] X. Zhang, J. Zhang, X. Ren, X.J. Wang, The dependence of persistent phosphorescence on annealing temperatures in $CaTiO_3$: Pr^{3+} nanoparticles prepared by a coprecipitation technique, J. Solid State Chem. 181 (2008) 393-398.

[9] V. Berbenni, A. Marini, Mechanical activation of calcium titanate formation from $CaCO_3$ TiO_2 mixtures, J. Mater. Sci. 39 (2004) 5279-5282.

ACCEPTED MANUSCRIPT

[10] H. Zhang, G. Chen, X. He, J. Xu, Electronic structure and photocatalytic properties of Ag-La codoped $CaTiO_3$, J. Alloy. Compd. 516 (2012) 91-95.

[11] H. Zhang, G. Chen, Y. Li, Y. Teng, Electronic structure and photocatalytic properties of copper-doped $CaTiO_3$, INT J. Hydrogen Energ. 35 (2010) 2713-2716.

[12] Y.S. Huo, H. Yang, T. Xian, J.L. Jiang, Z.Q. Wei, R.S. Li, W.J. Feng, A polyacrylamide gel route to different-sized $CaTiO_3$ nanoparticles and their photocatalytic activity for dye degradation, J. Sol-Gel Sci. Techn. 71 (2014) 254-259.

[13] T. Kimijima, K. Kanie, M. Nakaya, A. Muramatsu, Hydrothermal synthesis of size- and shape-controlled $CaTiO_3$ fine particles and their photocatalytic activity, Cryst. Eng. Comm. 16 (2014) 5591-5597.

[14] W. Dong, G. Zhao, B. Song, G. Xu, J. Zhou, G. Han, Surfactant-free fabrication of $CaTiO_3$ butterfly-like dendrite via a simple one-step hydrothermal route, Cryst. Eng. Comm. 14 (2012) 6990-6997.

[15] D. Croker, M. Loan, B.K. Hodnett, Kinetics and Mechanisms of the Hydrothermal Crystallization of Calcium Titanate Species, Cryst. Growth Des. 9 (2009) 2207-2213.

[16] D. Wang, Z. Guo, Y. Chen, J. Hao, W. Liu, In Situ Hydrothermal Synthesis of nanolamellate $CaTiO_3$ with Controllable Structures and Wettability, Inorg. Chem. 46 (2007) 7707-7709.

[17] H. Zhao, Y. Duan, X. Sun, Synthesis and characterization of $CaTiO_3$ particles with controlled shape and size, New J. Chem. 37 (2013) 986-991.

[18] X. Yang, J. Fu, C. Jin, J. Chen, C. Liang, M. Wu, W. Zhou, Formation Mechanism of $CaTiO_3$ Hollow Crystals with Different Microstructures, J. Am. Chem. Soc. 132 (2010) 14279-14287.

[19] J. Zhuang, Q. Tian, S. Lin, W. Yang, L. Chen, P. Liu, Precursor morphology-controlled formation of perovskites $CaTiO_3$ and their photo-activity for As(III) removal, Appl. Catal. B: Environ. 156-157 (2014) 108-115.

[20] S. Liu, Y. Qu, R. Li, G. Wang, Y. Li, Photocatalytic activity of $MTiO_3$ (M = Ca, Ni, and Zn) nanocrystals for water decomposition to hydrogen, J. Mater. Res. 29 (2014) 1295-1301.

[21] J.S. Jang, P.H. Borse, J.S. Lee, K.T. Lim, O.S. Jung, E.D. Jeong, J.S. Bae, H.G. Kim,

ACCEPTED MANUSCRIPT

Photocatalytic Hydrogen Production in Water-Methanol Mixture over Iron-doped $CaTiO_3$, B. Korean Chem. Soc. 32 (2011) 95-99.

[22] S. Otsuka-Yao-Matsuo, T. Omata, S. Ueno, M. Kita, Photobleaching of Methylene Blue Aqueous Solution Sensitized by Composite Powders of Titanium Oxide with $SrTiO_3$, $BaTiO_3$, and $CaTiO_3$, Mater. Trans. 44 (2003) 2124-2129.

[23] H. Mizoguchi, K. Ueda, M. Orita, S.C. Moon, K. Kajihara, M. Hirano, H. Hosono, Decomposition of water by a $CaTiO_3$ photocatalyst under UV light irradiation, Mater. Res. Bull. 37 (2002) 2401-2406.

[24] F.V. Motta, A.P.A. Marques, M.T. Escote, D.M.A. Melo, A.G. Ferreira, E. Longo, E.R. Leite, J.A. Varela, Preparation and characterizations of $Ba_{0.8}Ca_{0.2}TiO_3$ by complex polymerization method (CPM), J. Alloy. Compd. 465 (2008) 452-457.

[25] L. Dong, Q. Luo, K. Cheng, H. Shi, Q. Wang, W. Weng, W.Q. Han, Facet-specific assembly of proteins on $SrTiO_3$ polyhedral nanocrystals, Sci. Rep. 4 2014 5084.

[26] M. Shivaram, H. Nagabhushana, S.C. Sharma, S.C. Prashantha, B. Daruka Prasad, N. Dhananjaya, R. Hari Krishna, B.M. Nagabhushana, C. Shivakumara, R.P. Chakradhar, Synthesis and luminescence properties of Sm^{3+} doped $CaTiO_3$ nanophosphor for application in white LED under NUV excitation. Spectrochim, Acta Part A 128 (2014) 891-901.

[27] T. Phongamwong, M. Chareonpanich, J. Limtrakul, Role of chlorophyll in Spirulina on photocatalytic activity of CO_2 reduction under visible light over modified N-doped TiO_2 photocatalysts, Appl. Catal. B: Environ. 168-169 (2015) 114-124.

[28] Y.C. Zhang, M. Yang, G. Zhang, D.D. Dionysiou, HNO_3-involved one-step low temperature solvothermal synthesis of N-doped TiO_2 nanocrystals for efficient photocatalytic reduction of Cr(VI) in water, Appl. Catal. B: Environ. 142-143 (2013) 249-258.

[29] D.H. Wang, L. Jia, X.L. Wu, L.Q. Lu, A.W. Xu, One-step hydrothermal synthesis of N-doped TiO_2/C nanocomposites with high visible light photocatalytic activity, Nanoscale 4 (2012) 576-84.

[30] M.R. Waterland, A. Myers Kelley, Far-ultraviolet resonance Raman spectroscopy of nitrate ion in solution, J. Chem. Phys. 113 (2000) 6760-6773.

ACCEPTED MANUSCRIPT

[31] H. Tanak, M.K. Marchewka, FT-IR, FT-Raman, and DFT computational studies of melaminium nitrate molecular–ionic crystal, J. Mol. Struct. 1034 (2013) 363-373.

[32] H. Zheng, G.D.C. Csete de Györgyfalva, R. Quimby, H. Bagshaw, R. Ubic, I.M. Reaney, J. Yarwood, Raman spectroscopy of B-site order–disorder in $CaTiO_3$-based microwave ceramics, J. Eur. Ceram. Soc. 23 (2003) 2653-2659.

[33] M.L. Moreira, E.C. Paris, G.S. do Nascimento, V.M. Longo, J.R. Sambrano, V. R. Mastelaro, M.I.B. Bernardi, J. Andrés, J.A. Varela, E. Longo, Structural and optical properties of $CaTiO_3$ perovskite-based materials obtained by microwave-assisted hydrothermal synthesis: An experimental and theoretical insight, Acta Mater. 57 (2009) 5174-5185.

[34] B.J.M. Rajkumar, V. Ramakrishnan, Infrared and Raman spectra of L-valine nitrate and L-leucine nitrate, J. Raman Spectrosc. 31 (2000) 1107-1112.

[35] L.F. Faria, T.C. Penna, M.C. Ribeiro, Raman spectroscopic study of temperature and pressure effects on the ionic liquid propylammonium nitrate, J. Phys. Chem. B 117 (2013) 10905-10912.

[36] G. Zhang, Y.C. Zhang, M. Nadagouda, C. Han, K. O'Shea, S.M. El-Sheikh, A.A. Ismail, D.D. Dionysiou, Visible light-sensitized S, N and C co-doped polymorphic TiO_2 for photocatalytic destruction of microcystin-LR, Appl. Catal. B: Environ. 144 (2014) 614-621.

[37] A.G. Dylla, K.J. Stevenson, Electrochemical and Raman spectroscopy identification of morphological and phase transformations in nanostructured TiO_2(B), J. Mater. Chem. A 2 (2014) 20331-20337.

[38] C. Qiu, H. Zhou, B. Cao, L. Sun, T. Yu, Raman spectroscopy of morphology-controlled deposition of Au on graphene, Carbon 59 (2013) 487-494.

[39] Y. Tan, X. Zang, J. Gu, D. Liu, S. Zhu, H. Su, C. Feng, Q. Liu, W.M. Lau, W.J. Moon, D. Zhang, Morphological effects on surface-enhanced Raman scattering from silver butterfly wing scales synthesized via photoreduction, Langmuir 27 (2011) 11742-11746.

[40] M. Nasir, S. Bagwasi, Y. Jiao, F. Chen, B. Tian, J. Zhang, Characterization and activity of the Ce and N co-doped TiO_2 prepared through hydrothermal method, Chem. Eng. J. 236 (2014) 388-397.

ACCEPTED MANUSCRIPT

[41] N. Shi, X. Li, T. Fan, H. Zhou, J. Ding, D. Zhang, H. Zhu, Biogenic N-I-codoped TiO_2 photocatalyst derived from kelp for efficient dye degradation, Energy Environ. Sci. 4 (2011) 172-180.

[42] D.L. Shieh, Y.S. Lin, J.H. Yeh, S.C. Chen, B.C. Lin, J.L. Lin, N-Doped, porous TiO_2 with rutile phase and visible light sensitive photocatalytic activity, Chem. Commun. 48 (2012) 2528-2530.

[43] J. Zhang, J. Xi, Z. Ji, Mo+N Codoped TiO_2 sheets with dominant {001} facets for enhancing visible-light photocatalytic activity, J. Mater. Chem. 22 (2012) 17700-17708.

[44] S. Hoang, S.P. Berglund, N.T. Hahn, A.J. Bard, C.B. Mullins, Enhancing visible light photo-oxidation of water with TiO_2 nanowire arrays via cotreatment with H_2 and NH_3: synergistic effects between Ti^{3+} and N, J. Am. Chem. Soc. 134 (2012) 3659-3662.

[45] C. Liu, T. Sun, L. Wu, J. Liang, Q. Huang, J. Chen, W. Hou, N-doped $Na_2Ti_6O_{13}$@TiO_2 core–shell nanobelts with exposed {101} anatase facets and enhanced visible light photocatalytic performance, Appl. Catal. B: Environ. 170-171 (2015) 17-24.

[46] S. Hu, F. Li, Z. Fan, J. Gui, Improved photocatalytic hydrogen production property over Ni/NiO/N-TiO_{2-x} heterojunction nanocomposite prepared by NH_3 plasma treatment, J. Power Sources 250 (2014) 30-39.

[47] J. Liu, R. Han, Y. Zhao, H. Wang, W. Lu, T. Yu, Y. Zhang, Enhanced Photoactivity of V-N Codoped TiO_2 Derived from a Two-Step Hydrothermal Procedure for the Degradation of PCP-Na under Visible Light Irradiation, J. Phys. Chem. C 115 (2011) 4507-4515.

[48] X. Chen, X. Wang, Y. Hou, J. Huang, L. Wu, X. Fu, The effect of postnitridation annealing on the surface property and photocatalytic performance of N-doped TiO_2 under visible light irradiation, J. Catal. 255 (2008) 59-67.

[49] X. Yang, C. Cao, L. Erickson, K. Hohn, R. Maghirang, K. Klabunde, Synthesis of visible-light-active TiO_2-based photocatalysts by carbon and nitrogen doping, J. Catal. 260 (2008) 128-133.

[50] J. Wang, D.N. Tafen, J.P. Lewis, Z. Hong, A. Manivannan, M. Zhi, M. Li, N. Wu, Origin of Photocatalytic Activity of Nitrogen-Doped TiO_2 Nanobelts, J. Am. Chem. Soc. 131 (2009) 12290-12297.

ACCEPTED MANUSCRIPT

[51] R. Nakamura, T. Tanaka, Y. Nakato, Mechanism for Visible Light Responses in Anodic Photocurrents at N-Doped TiO_2 Film Electrodes, J. Phys. Chem. B 108 (2004) 10617-10620.

[52] R. Asahi, T. Morikawa, T. Ohwaki, K. Aoki, Y. Taga, Visible-Light Photocatalysis in Nitrogen-Doped Titanium Oxides, Science 293 (2001) 269-271.

[53] R.A.R. Monteiro, S.M. Miranda, V.J.P. Vilar, L.M. Pastrana-Martínez, P.B. Tavares, R.A.R. Boaventura, J.L. Faria, E. Pinto, A.M.T. Silva, N-modified TiO_2 photocatalytic activity towards diphenhydramine degradation and Escherichia coli inactivation in aqueous solutions, Appl. Catal. B: Environ. 162 (2015) 66-74.

Table 1 Crystallite sizes, specific surface areas, and bandgaps of not-acidified and acidified $CaTiO_3$ particles

Samples	Crystalline grain sizes	Specific surface areas	Band gaps
$CaTiO_3$	43.5 nm	16.92 m^2/g	3.50 eV
$CaTiO_3$(pH=4)	43.2 nm	17.39 m^2/g	3.46 eV
$CaTiO_3$(pH=2)	43.9 nm	16.14 m^2/g	3.42 eV
$CaTiO_3$(2 mol/L)	43.4 nm	14.90 m^2/g	3.51 eV